Local geometry of a weak normal shock wave interacting with turbulence

Amane Kusuhata (楠畑 天音),[1] Kento Tanaka (田中 健人),[2] Tomoaki Watanabe (渡邉 智昭),[3, a)] Koji Nagata (長田 孝二),[4] and Akihiro Sasoh (佐宗 章弘)[3]

[1)] *Department of Aerospace Engineering, Nagoya University, Nagoya, Japan*

[2)] *Faculty of Natural Science and Technology, Okayama University, Tsushimanaka 3-1-1, Kita, Okayama, Okayama 700-8530, Japan*

[3)] *Education and Research Center for Flight Engineering, Nagoya University, Furo-cho, Chikusa, Nagoya, 464-8603, Japan*

[4)] *Department of Mechanical Engineering and Science, Kyoto University, Kyoto 615-8530, Japan*

(Dated: 4 July 2023)

Local geometry of a weak normal shock wave interacting in turbulence

The shock surface geometry is investigated with direct numerical simulations of a weak normal shock wave propagating in turbulence. The geometry is quantified with the principal curvatures of the surface. A large part of the surface has an approximately-flat saddle shape while elliptic concave and convex shapes with a large curvature intermittently appear on the shock surface. The pressure-dilatation correlation in the governing equation of pressure is investigated at the shock wave with the decomposition into three terms associated with the velocity gradients in the two directions of the principal curvatures and the normal direction of the shock wave. Fluid expansion in the tangential direction occurs at the shock wave with a convex shape in the direction of the shock propagation, resulting in a smaller pressure jump across the shock wave. For a concave shape, compression in the tangential direction can amplify the pressure jump. Consistently, small and large shock Mach numbers are observed for convex and concave shapes, respectively. The geometric influences are the most significant for elliptic concave and convex shapes with approximately equal curvatures in the two principal directions because the compression or expansion occurs in all tangential directions. These relations between the shock surface geometry and shock Mach number observed in turbulence are consistent with the theory of deformed shock waves, suggesting that the three-dimensional geometrical features of the shock surface are important in the modulation of shock waves due to turbulence.

[a)]Author to whom correspondence should be addressed: watanabe.tomoaki@c.nagoya-u.jp

Local geometry of a weak normal shock wave interacting in turbulence

I. INTRODUCTION

Shock waves are observed in various scientific and engineering fields, such as inertial fusion,[1] supernova explosion[2], supersonic aircraft,[3] and detonation engines.[4] For the supersonic aircraft, the generated shock waves are observed as a big noise called sonic boom, which may have significant influences on the environment.[5] Observations have confirmed that the sonic boom is influenced by atmospheric turbulence.[6] Predicting the sonic boom level requires accurate modeling of the modulation of the shock wave due to turbulence.[7] Similarly, shock waves propagating in turbulence are widely observed because flows easily become turbulent due to various flow instabilities. The interaction has been studied for a shock wave propagating in isotropic turbulence, which is one of the simplest problems of the shock/turbulence interaction, as reviewed below. Another practically-important example is the interaction of shock waves with a turbulent boundary layer, which is often observed in a high-speed flow over an airfoil.[8] The statistical inhomogeneity of the boundary layer and the wall influences result in a very complicated flow field with multiple shock waves and flow separation.[9,10]

The propagation of shock waves in turbulence affects the properties of both shock waves and turbulence. The interaction between shock waves and turbulence has been studied with theoretical analyses, experiments, and numerical simulations. The characteristic length, velocity, and time scales of turbulence change when turbulence undergoes strong compression due to the shock wave. The theoretical studies have been devoted to predicting the statistical properties of turbulence behind a shock wave as functions of a shock Mach number and turbulence characteristics in front of the shock wave. These studies often rely on linearized equations, e.g., a linear interaction analysis (LIA)[11–13] and rapid distortion theory (RDT),[14–16] which enable us to derive analytical or numerical solutions for simplified problems. Experiments and numerical simulations of shock waves propagating in turbulence have been compared with these theoretical studies, which sometimes provide good predictions for the statistics of turbulence behind the shock waves. The LIA and RDT predict that velocity fluctuations in the normal direction to the shock wave are amplified by the interaction. The amplification of the velocity fluctuations is indeed observed in experiments of shock waves interacting with grid turbulence in a shock tube[17,18] and wind tunnel.[19] and in numerical simulations of statistically steady normal shock waves in isotropic turbulence.[20–22] and un-

steady cases.[23] Most of these studies alao confirmed that the integral scales of turbulence often decrease by the interaction with shock waves.

Shock waves are also strongly influenced by turbulence although this influence is less understood than the changes in turbulence due to the shock waves. A shock wave causes distinct jumps of flow variables, which are related to the shock Mach number with the Rankine–Hugoniot relations. Direct numerical simulations (DNS) of a normal shock wave in turbulence revealed that the density and pressure jumps across the shock wave exhibit fluctuations when interacting with turbulence.[21,23] Similarly, experimental studies also reported that fluctuations in the pressure jump were induced by turbulence for spherical shock waves in a turbulent jet,[24] grid turbulence,[25,26] and turbulent wake.[27] These studies of canonical shock/turbulence interaction qualitatively agree with the observation of sonic booms influenced by atmospheric turbulence. Another influence of turbulence is observed for the shock-surface geometry. The deformation of shock waves was experimentally confirmed in the visualization of a spherical shock wave in a turbulent jet[24] and a normal shock wave in grid turbulence.[28] DNS studies of a normal shock wave in homogeneous isotropic turbulence also reported that the shock wave can be broken by turbulence with large velocity fluctuations[21] whereas they deform without being broken for small velocity fluctuations.[29]

The modulation of shock waves by turbulence has also been discussed in theoretical works. A shockfront-folding mechanism was proposed as a theoretical explanation of measured rise time in sonic-boom pressure.[30] The shock-wave vanishment in turbulence was discussed with a one-dimensional model of a shock wave propagating in forward flow.[31] Other studies explain the statistical behaviour of shock waves interacting with turbulence with the shock wave deformation due to a non-uniform velocity profile as explained below.[32,33] A shock wave is known to be locally strengthened for a concave shape in the propagation direction whereas it is weakened for a convex shape.[34] These behaviors of the deformed shock waves are related to converging and diverging shock rays. They cause focusing and defocusing effects, which can amplify and attenuate the shock wave, respectively. The shock wave deformation can be caused by turbulent velocity fluctuations. At a certain point on the shock wave, the velocity for the movement of the shock wave is expressed by the sum of the shock propagation velocity and the fluid velocity at which the shock wave is located. The former is determined by the local shock Mach number and the speed of sound while the latter fluctuates in turbulence. Therefore, the velocity of the shock wave movement becomes non-

uniform in turbulent flows, where the fluid velocity varies with time and position. The non-uniform velocity of the shock movement results in the deformation of the shock surface. A simplified model based on the shock wave deformation due to this non-uniform velocity was considered in Inokuma et al.[32,33] Some important consequences of the model are as follows. Once the shock wave deforms, the local shock rays do not align with the original propagation direction. The converging and diverging rays caused by the deformation locally amplify and attenuate the shock wave, respectively.[34] Because it takes time for the shock wave to deform after the velocity of the shock wave movement becomes non-uniform, the effects of velocity fluctuations gradually prevail for the shock wave. The model also predicts that the normalized root-mean-squared (rms) value of pressure-jump fluctuations of shock waves, $\Delta P'_{rms}/\langle \Delta P \rangle = \sqrt{\langle \Delta P^2 \rangle - \langle \Delta P \rangle^2}/\langle \Delta P \rangle$, where $\langle \quad \rangle$ denotes an average defined as ensemble averages of repeated experiments or averages on shock surface and ΔP is a local pressure jump across a shock wave, is given as a function of the shock Mach number M_{S0} and turbulent Mach number M_{T0} before the interaction. Specifically, $\Delta P'_{rms}/\langle \Delta P \rangle \sim [M_{T0}^2/(M_{S0}^2 - 1)]^{1/2}$ and $\Delta P'_{rms}/\langle \Delta P \rangle \sim M_{T0}/M_{S0}$ have been derived as the asymptotic solutions of weak and strong shock waves, respectively. The model based on the shock wave deformation successfully explains experimental and numerical observations of shock waves in turbulence. The response time in the shock wave modulation was confirmed with a correlation analysis between the pressure jump of shock waves and turbulent velocity fluctuations in experiments[26,32] and numerical simulations.[23] Furthermore, data compiled from various experiments and numerical simulations successfully recover $\Delta P'_{rms}/\langle \Delta P \rangle \sim [M_T^2/(M_{S0}^2 - 1)]^{1/2}$ for weak shock waves.[33]

These studies suggest the importance of the shock surface geometry in understanding the influence of turbulence on the shock wave. In experimental studies, the deformation of shock waves interacting with turbulence is often evaluated with shadowgraph or Schlieren images. Although these visualizations do not reveal the local geometry of the shock wave, they are useful to assess the degree of deformation. Visualization of a spherical shock wave disturbed by a turbulent jet was carried out together with pressure measurements for the shock wave.[24]. They observed that when the disturbed shock wave was located behind the location expected for the undisturbed shock wave, the shock wave exhibited a significantly large pressure jump, which implied that the shock wave was strengthened by the turbulent jet. An opposite effect was observed for the disturbed shock wave located ahead of the

undisturbed one. DNS studies of a normal shock wave also examined the shock wave deformation by the relative position of the shock wave to the mean position.[21,29,35] The correlation between the shock position and the pressure and density jumps across the shock wave in these simulations is consistent with the experiments mentioned above. Fourier analyses have shown that the local shock position characterizes the large-scale deformation of the shock wave.[29] However, visualization has also revealed the existence of small-scale wrinkles on the shock surface in numerical simulations[21,29] and experiments.[36] These small-scale geometrical features are unlikely to be related to the local shock position. However, the shock deformation model implies that the concave and convex shapes associated with the small-scale wrinkles are also relevant to local amplification and attenuation of the shock wave caused by turbulence.[32,33] Nonetheless, the small-scale features of the shock wave deformation have hardly been explored in the existing literature on canonical shock/turbulence interaction. In the present study, this is investigated with DNS database of a weak normal shock wave propagating in homogeneous isotropic turbulence.[29] Here, "weak" means that $\Delta P'_{rms}/\langle \Delta P \rangle$ follows the scaling for weak shock waves.[33] A new post-processing procedure is proposed for the evaluation of the shock-surface geometry with local curvatures. Our previous paper with the same DNS database investigated the large-scale deformation of shock waves, which is related to large-scale turbulent motion.[29] On the other hand, the local curvatures can capture the small-scale geometry, which is possibly related to small-scale turbulent motion. Turbulence has very different properties between large and small scales. Therefore, it is important to investigate both large- and small-scale geometry of the shock wave interacting with turbulence. The local geometry of the shock wave are evaluated by the mean curvature and Gaussian curvature, which are widely used to investigate the geometry of various surfaces in turbulent flows, such as scalar isosurface in turbulence[37] and turbulent/non-turbulent interface in jets,[38,39] mixing layers,[40] and shear-free turbulence.[41] The relationship is investigated for the curvatures to the local shock Mach number, whose fluctuations are also investigated with the analysis of the internal energy equation.

The present study considers the deformation of the shock wave, which occurs when turbulence is not strong enough for the shock wave to be broken. The interaction with turbulence at a sufficiently large turbulent Mach number generates holes on the shock surface,[20] which are not investigated in this study. In addition, mean shear is absent in homogeneous isotropic turbulence considered in this study although its influence on shock waves is practically im-

portant. Turbulent shear flows often contain large-scale coherent structures arising from shear instability. However, these structures are known to be absent in turbulence without mean shear.[42] The large-scale structures may affect the propagation of shock waves in turbulent shear flows. Experiments of a shock wave propagating in a turbulent jet have confirmed that the mean shear of the jet affects the pressure jump across the shock wave.[43] A similar effect has also been observed for a shock wave in a turbulent cylinder wake.[27] In past decades, proper orthogonal decomposition[44] and dynamic mode decomposition[45] have proved useful for the identification of large-scale structures in turbulent shear flows, as confirmed for planar jets,[46] axisymmetric jets,[47] mixing layers,[48] wall-confined shear flows,[49] and cylinder wakes.[50] These studies have confirmed various types of coherent structures that dominate large-scale velocity fluctuations of turbulence. The influences of these large-scale structures on shock waves may be better studied with numerical simulations combined with the identification schemes of flow structures. The mean shear effects are related to more practical problems and should be addressed in future studies while the present DNS considers one of the simplest problems with turbulence without mean shear.

The paper is organized as follows. Section II presents the details of the DNS database of the normal shock wave propagating in turbulence. The post-processing procedure to assess the local geometry of the shock wave is presented in Sec. III. Section IV discusses the statistical properties of the curvatures and their relation to the local shock Mach number. In addition, how the shock wave is amplified or attenuated on the wrinkled surface is examined with the internal energy equation evaluated on the shock surface. Finally, the paper is summarized in Sec. V.

II. DNS DATABASE OF A NORMAL SHOCK WAVE PROPAGATING IN A LOCAL TURBULENT REGION

The DNS database of a normal shock wave propagating in a local turbulent region is briefly described below while a previous paper provides detailed descriptions.[29] Figure 1 shows the overview of the initial condition of the DNS. Homogeneous isotropic turbulence taken from another DNS is inserted in the middle of the quiescent fluid. The turbulent and quiescent regions are smoothly connected by a window function defined with a hyperbolic tangent function.[51,52] The DNS of isotropic turbulence was carried out with a linear forcing

Local geometry of a weak normal shock wave interacting in turbulence

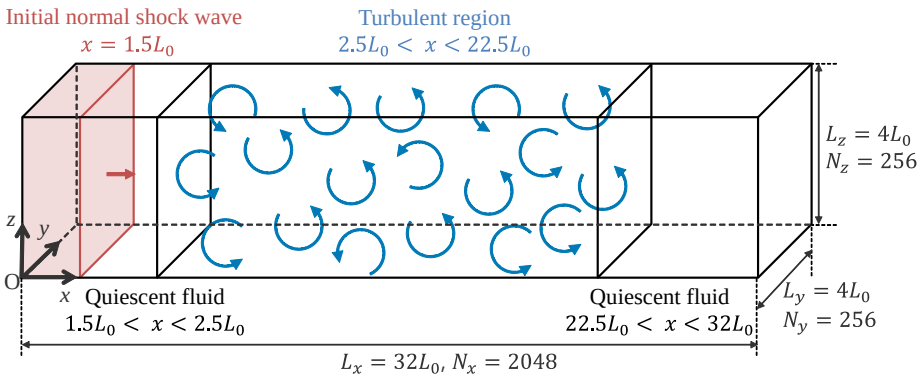

FIG. 1. DNS of a normal shock wave propagating in a local turbulent region.[29]

scheme.[53] The normal shock wave is initially located in the quiescent fluid region, where the shock wave initially propagates. The shock wave begins to interact with turbulence once it reaches the turbulent region. Time is advanced until the shock wave reaches $x/L_0 = 19$, which is close to the end of the turbulent region.

The governing equations are three-dimensional compressible Navier–Stokes equations with the equation of state for a perfect gas, as shown below:

$$\frac{\partial \rho}{\partial t} + \frac{\partial \rho u_j}{\partial x_j} = 0, \tag{1}$$

$$\frac{\partial \rho u_i}{\partial t} + \frac{\partial (\rho u_i u_j + \delta_{ij} P)}{\partial x_j} = \frac{\partial \tau_{ij}}{\partial x_j}, \tag{2}$$

$$\frac{\partial \mathcal{E}}{\partial t} + \frac{\partial (\mathcal{E} + P) u_j}{\partial x_j} = \frac{\partial \tau_{ij} u_i}{\partial x_j} + \frac{\partial}{\partial x_j}\left(k_T \frac{\partial T}{\partial x_j}\right), \tag{3}$$

$$P = \rho R T, \tag{4}$$

where t is time, x_i is the i-th spatial coordinate, ρ is the density, u_i is the i-directional velocity, $\mathcal{E} = P/(\gamma - 1) + \rho u_i^2/2$ is the total energy, T is the temperature, P is the pressure, μ is the viscosity coefficient calculated according to Sutherland's law, k_T is the thermal conductivity, δ_{ij} is the Kronecker delta, and τ_{ij} is the shear stress tensor expressed as

$$\tau_{ij} = \mu\left(\frac{\partial u_i}{\partial x_j} + \frac{\partial u_j}{\partial x_i} - \frac{2}{3}\delta_{ij}\frac{\partial u_k}{\partial x_k}\right). \tag{5}$$

The working fluid is air with the gas constant $R = 287$ J/(kg K) and the specific heat ratio $\gamma = 1.4$. The Prandtl number is $Pr = 0.71$, which relates μ to k_T. The DNS code is based on a finite volume method with a shock-capturing scheme. Spatial discretization of inviscid terms is based on Roe-flux difference splitting with a fifth-order weighted essentially non-oscillatory (WENO) scheme. The other terms are calculated with a sixth-order central difference scheme. Time advancement is based on the four-stage and fourth-order Runge–Kutta method. The same code was used in our previous studies of shock waves interacting with turbulence,[23,29] where the DNS results were compared with experiments, other DNS, and theories of the shock/turbulence interaction. For example, an amplification factor of turbulent kinetic energy by the shock wave was shown to agree with the LIA.[23]

The size of the computational domain is described as $(L_x, L_y, L_z) = (32L_0, 4L_0, 4L_0)$ with a reference scale L_0. Before the DNS of the shock wave propagation in turbulence, an additional DNS is conducted to simulate homogeneous isotropic turbulence, which is used for generating the initial condition of the main simulations. The initial condition for isotropic turbulence is solenoidal velocity fluctuations, which are generated by applying an inverse Fourier transform to velocity vectors in wavenumber space with a prescribed energy spectrum and random phases.[29] The reference scale L_0 is taken as an integral scale of the initial condition for homogeneous isotropic turbulence and is defined as $L_0 = (\sqrt{3/2}u_0)^3/\varepsilon_0$, where $u_0 = \sqrt{\langle u^2\rangle_V - \langle u\rangle_V^2}$ is the rms velocity fluctuations, $\varepsilon_0 = \langle 2\nu S_{ij}S_{ij}\rangle_V$ is the kinetic energy dissipation rate, ν is the kinematic viscosity, $S_{ij} = (\partial u_i/\partial x_j + \partial u_j/\partial x_i)/2$ is the rate-of-strain rate, and $\langle f\rangle_V$ is a volume average of f in isotropic turbulence. The integral length scale of the initial condition of the shock/turbulence interaction is about $0.7L_0$, as shown in Tanaka et al.[29]

The boundary conditions at $x = 0$ assume fixed values for velocity, pressure, and temperature determined with the Rankine–Hugoniot relations and the shock Mach number. Zero-gradient boundary conditions are applied to the boundary at $x = 32L_0$. The flow is statistically homogeneous in the y and z directions, for which the periodic boundary conditions are applied.

The main parameters of the flow at the initial condition are the shock Mach number M_{S0}, turbulent Mach number $M_{T0} = \sqrt{3}u'_{rms0}/a_0$, and turbulent Reynolds number $Re_{\lambda 0} = \rho_0 u'_{rms0}\lambda_{x0}/\mu_0$. Here, subscript 0 indicates values in the turbulent region at the initial condition, f' denotes fluctuations of variable f, u'_{rms0} is the rms velocity fluctua-

tions in the x direction, and $\lambda_{x0} = u'_{rms0}/(\partial u'/\partial x)_{rms0}$ is the Taylor microscale defined with the rms fluctuations of the longitudinal velocity gradient, $(\partial u'/\partial x)_{rms0}$. These quantities are evaluated with volume averages taken in the turbulent region. The speed of sound a_0, density ρ_0, and viscosity coefficient μ_0 are also evaluated as the mean properties of the fluid in turbulence. The initial mean pressure and temperature in front of the shock wave are 1.013×10^5 Pa and 300 K, respectively, while their values behind the shock wave are determined with the Rankine–Hugoniot relations. The DNS database is analyzed for four cases: $(M_{S0}, M_{T0}) = (1.3, 0.13)$, $(1.3, 0.063)$, $(1.3, 0.011)$, and $(1.1, 0.011)$. For all cases, the turbulent Reynolds number is about 60.

The number of the computational grid points is $(N_x, N_y, N_z) = (2048, 256, 256)$, which gives a grid spacing of about 1.4 times the Kolmogorov scale in three directions. The grid-dependence test confirmed that the grid spacing was sufficiently small for the behaviors of the shock wave and turbulence to be independent of the resolution.[29] The time increment Δt is determined with a constant Courant–Friedrichs–Lewy number (CFL) of CFL = 0.6 as

$$\Delta t = \mathrm{CFL} \times \min\left[\left\{\left(\frac{|u|}{\Delta x} + \frac{|v|}{\Delta y} + \frac{|w|}{\Delta z}\right) + \sqrt{\gamma R T\left(\frac{1}{\Delta x^2} + \frac{1}{\Delta y^2} + \frac{1}{\Delta z^2}\right)}\right\}^{-1}\right], \quad (6)$$

where $\Delta x = \Delta y = \Delta z$ is the grid spacing in each direction and the minimum value is taken from the computational domain at each time step. This calculation of the time increment based on fluid velocity and local speed of sound was also used in other simulations of compressible turbulence.[54,55] The time increment in the present DNS hardly changes with time because the mean shock Mach number does not change with the propagation in turbulence.[23] For $(M_{S0}, M_{T0}) = (1.3, 0.13)$, $(1.3, 0.063)$, $(1.3, 0.011)$, and $(1.1, 0.011)$, the typical values of Δt normalized by the integral time scale defined as the ratio between the rms velocity fluctuation and the integral scale are 2.3×10^{-4}, 1.2×10^{-4}, 2.3×10^{-5}, and 2.8×10^{-5}, respectively.

The values of M_{S0} in the present DNS are chosen to investigate weak shock waves. From an early theoretical work of shock waves, weak and strong shock waves are expected to behave differently in turbulence.[56] A theoretical model also predicts that the scaling law of pressure-jump fluctuations is different for weak and strong shock waves as also discussed in Sec. I: $\Delta P'_{rms}/\langle \Delta P \rangle \sim [M_{T0}^2/(M_{S0}^2 - 1)]^{1/2}$ for weak shock waves and $\Delta P'_{rms}/\langle \Delta P \rangle \sim M_{T0}/M_{S0}$ for strong shock waves. The scaling for strong shock waves is expected to be valid when M_{S0} exceeds about 3 although it is not confirmed yet in experiments. On the other hand, the

scaling for weak shock waves has been observed in experiments and numerical simulations for $1.0009 \lesssim M_{S0} \lesssim 1.5$, for which the mechanism of the shock wave modulation by turbulence is expected to be unchanged.[33] The present findings for the weak shock waves are expected to be valid at least for this range of M_{S0}. The turbulent Mach number is chosen for quantitative comparisons of the present DNS with experiments. For numerical simulations of shock waves, this is important because the shock waves are treated with a shock-capturing scheme which introduces numerical diffusion. Here, M_{T0} is determined such that $M_{T0}^2/(M_{S0}^2-1)$ falls within the range of $M_{T0}^2/(M_{S0}^2-1) = O(10^{-5})$–$O(10^{-2})$, for which experiments have been conducted with pressure measurements of weak shock waves, as summarized in Inokuma et al.[33] A comparison with the experiments will be presented in Sec. III C, validating the DNS and post-processing procedure.

The present DNS considers a moderately large Reynolds number, $Re_\lambda \approx 60$. Turbulence possesses statistically universal features of small-scale velocity fluctuations, such as a shape of a kinetic energy spectrum at high wavenumbers.[57] This universarlity of the spectral shape is not valid in low-Re_λ turbulence when $Re_\lambda \lesssim 20$.[58] The small-scale velocity fluctuations in the present DNS with $Re_\lambda \approx 60$ are expected be statitsically similar to those for higher Re_λ. The small-scale geometry of the shock wave is investigated in this study. Previous studies have shown that the large-scale geometry of shock waves propagating in turbulence has a characteristic length scale close to the integral scale of turbulence, which is a length scale of large-scale turbulent motion.[29] These length scales of the shock wave deformation and turbulence imply that the small-scale geometry of shock waves is related to small-scale velocity fluctuations in turbulence. If this is the case, the present results will also be useful in understanding shock waves propagating in high-Re_λ turbulent flows, although this issue should be carefully examined in future studies.

Figure 2 visualizes an instantaneous flow field with the two-dimensional distribution of the magnitude of velocity vectors $|\boldsymbol{u}|$ for $(M_S, M_T) = (1.3, 0.063)$ at an instance when the shock wave is propagating in the turbulent region. The shock wave was initially located at $x/L_0 = 1.5$ in the non-turbulent region and propagated in the x direction. Once the shock wave reaches the turbulent region, their interaction occurs. Because of the induced flow of the shock wave, the velocity becomes large behind the shock wave. In Fig. 2, the length of the non-turbulent region for the side of $x = 0$ is larger than the initial length because the shock-induced mean flow in the x direction advects the turbulent region. For

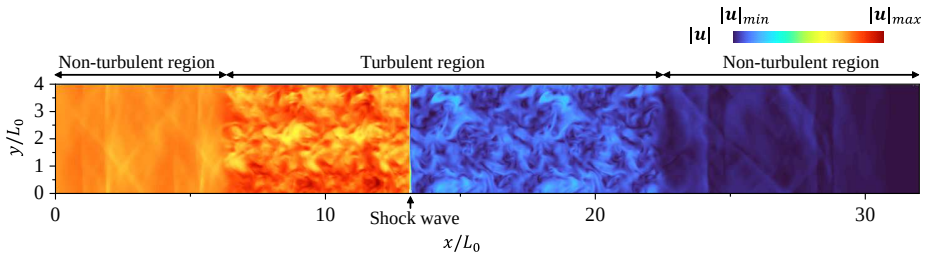

FIG. 2. Two-dimensional distribution of the magnitude of velocity vectors $|\boldsymbol{u}|$ for $(M_S, M_T) = (1.3, 0.063)$. The shock wave is located at $x/L_0 \approx 13$. The color range corresponds to the maximum and minimum values of $|\boldsymbol{u}|$.

the present conditions, the interaction is not strong enough for the shock wave to be broken by turbulence. Therefore, the shock wave retains its wavefront during the propagation in turbulence. In addition, although the shock wave exhibits fluctuations in the shock Mach number in turbulence, the statistical properties of the shock wave become stationary in all simulations once it propagates in turbulence for a sufficiently long time, as discussed in Tanaka et al.[29]

III. STATISTICAL ANALYSES OF THE SHOCK SURFACE GEOMETRY AND SHOCK MACH NUMBER

A. Local geometry of a shock surface

The DNS database is analyzed to investigate the local geometry of the shock surface and its relation to the modulation of the shock wave due to turbulence. Here, we describe the post-processing procedure applied to the present database.

The local geometry of the shock wave is quantified with curvatures defined for a surface.[37] The following procedure is applied to a snapshot of the DNS at a given time, and the variables are also given as functions of time although this time dependence is not explicitly specified. The analysis presented below is repeatedly conducted for all snapshots. To begin with, the shock surface is identified with the local shock position following Tanaka et al.[29]. The shock surface is represented by the local shock position which is a function of (y, z) in a single

snapshot at a fixed time. At each position of (y, z), the x coordinate of the shock position, $x_S(y, z)$, is identified with a pressure gradient plotted against x at (y, z). Because of the strong compression in the shock normal direction, $\partial P/\partial x$ takes a large negative value at the shock wave. The local shock position $x_S(y, z)$ is determined as the x position where $\partial P/\partial x$ attains the smallest value. Here, a second-order Lagrangian interpolation is used to determine x_S from $\partial P/\partial x$ defined at discrete points. This procedure for $\partial P/\partial x$ is repeatedly applied at different positions of (y, z) to construct the shock surface defined as $x_S(y, z)$.

The geometry of the shock surface is evaluated with the mean curvature H and Gaussian curvature K, which can be calculated with $x_S(y, z)$ as explained here and by Kobayashi.[59] The principal curvatures of a surface represent the maximum and minimum curvatures, which are denoted by κ_1 and κ_2, respectively ($\kappa_1 \geq \kappa_2$). For the shock surface $x_S(y, z)$, they are the eigenvalues of the following matrix

$$\boldsymbol{A} = \begin{bmatrix} L & M \\ M & N \end{bmatrix}, \tag{7}$$

where the elements of $\boldsymbol{A}$ provide the second fundamental form[59] of the shock surface as $II = Ldy^2 + 2Mdydz + Ndz^2$ and are given by

$$L = -\boldsymbol{e}_{yt} \cdot \frac{\partial \boldsymbol{e}_n}{\partial y}, \quad M = -\boldsymbol{e}_{yt} \cdot \frac{\partial \boldsymbol{e}_n}{\partial z}, \quad N = -\boldsymbol{e}_{zt} \cdot \frac{\partial \boldsymbol{e}_n}{\partial z}. \tag{8}$$

Here, $\boldsymbol{e}_{yt}(y, z)$ and $\boldsymbol{e}_{zt}(y, z)$ are the unit tangential vectors that align in the y and z directions, respectively, and $\boldsymbol{e}_n(y, z)$ is the unit normal vector. These vectors are defined with $x_S(y, z)$ as

$$\boldsymbol{e}_{yt} = \left(\left[1 + \left(\frac{\partial x_S}{\partial y} \right)^2 \right]^{-1/2}, \ \frac{\partial x_S}{\partial y} \left[1 + \left(\frac{\partial x_S}{\partial y} \right)^2 \right]^{-1/2}, \ 0 \right), \tag{9}$$

$$\boldsymbol{e}_{zt} = \left(\left[1 + \left(\frac{\partial x_S}{\partial z} \right)^2 \right]^{-1/2}, \ 0, \ \frac{\partial x_S}{\partial z} \left[1 + \left(\frac{\partial x_S}{\partial z} \right)^2 \right]^{-1/2} \right), \tag{10}$$

$$\boldsymbol{e}_n = \boldsymbol{e}_{yt} \times \boldsymbol{e}_{zt}. \tag{11}$$

The eigenvectors of $\boldsymbol{A}$ corresponding to each eigenvalue are denoted by (w_{1y}, w_{1z}) and (w_{2y}, w_{2z}), by which the principal directions, namely the directions of the principal curvatures, are obtained as

$$\boldsymbol{e}_{t1} = w_{1y}\boldsymbol{e}_{yt} + w_{1z}\boldsymbol{e}_{zt}, \tag{12}$$

$$\boldsymbol{e}_{t2} = w_{2y}\boldsymbol{e}_{yt} + w_{2z}\boldsymbol{e}_{zt}. \tag{13}$$

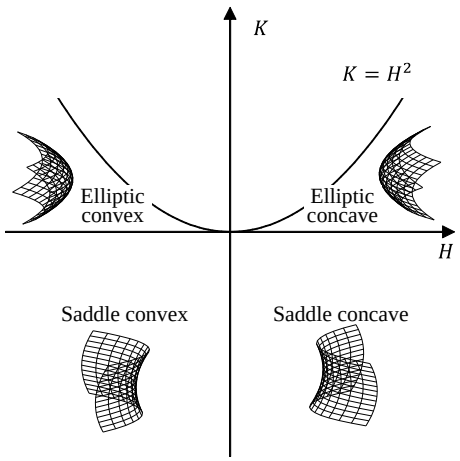

FIG. 3. Characterization of the local geometry of the shock surface with the mean and Gaussian curvatures, H and K.

The mean curvature H and Gaussian curvature K are defined with the principal curvatures as

$$H = \frac{1}{2}\left(\kappa_1 + \kappa_2\right), \tag{14}$$

$$K = \kappa_1 \kappa_2. \tag{15}$$

The shock wave observed from the propagation direction has concave and convex shapes in the $\boldsymbol{t}_i$ direction for positive and negative κ_i, respectively. The signs of H and K distinguish the shape of the surface. Figure 3 shows examples of the surface geometry for different (H, K). A flat surface has $(H, K) = (0, 0)$. The shock surface has concave and convex shapes for $H > 0$ and $H < 0$, respectively, while elliptic and saddle shapes are represented by $K > 0$ and $K < 0$, respectively. Thus, four types of surface shapes are represented in four quadrants. Examples of the surfaces are also illustrated in the figure. Here, the shock wave is assumed to propagate from left to right for the sketches of the surface. The surface does not satisfy $K > H^2$, which corresponds to complex curvatures.

B. Local shock Mach number

The local shock Mach number is also evaluated on the shock surface. The shock Mach number is related to the pressure jump across the shock wave caused by the compression in the propagation direction. Because of the deformation of the shock wave, this direction does not locally align with the x direction. Therefore, the pressure jump is evaluated on a one-dimensional coordinate ζ_n whose direction is given by $\boldsymbol{e}_n$. The local pressure jump is evaluated with a procedure used in the previous study.[23]. The coordinate ζ_n has its origin at (x_S, y, z), which is on the shock surface. The direction of ζ_n is taken in the normal direction $\boldsymbol{e}_n$ of the shock surface at (x_S, y, z). Here, positive ζ_n is on the front side of the shock wave. The coordinate ζ_n is discretized with a spacing smaller than the computational grid size. The pressure profile on the DNS grid, $P(x, y, z)$, is interpolated on ζ_n with a third-order Lagrangian interpolation scheme, providing $P(\zeta_n)$ across the shock surface at (x_S, y, z). The interpolation is repeatedly applied for ζ_n defined for different locations of the shock surface. Then, an average of P is conditionally taken as a function of ζ_n. This average is denoted by $P_A(\zeta_n)$. With the mean pressure values in front of and behind the shock wave, which are respectively denoted by P_F and P_B, the normalized pressure is defined as $\hat{P}(\zeta_n) = (P_A - P_F)/(P_B - P_F)$, which varies from 0 to 1 across the shock wave. Here, P_B and P_F are respectively evaluated as P_A at $\zeta_n = -L_0$ and L_0, which are far from the shock wave. Then, $\hat{P}$ is averaged over time in the statistically steady regime of the interaction. For the present DNS, the shock wave was shown to be statistically steady when it is located between $x = 13L_0$ and $19L_0$.[29] The location with the average of $\hat{P}$ being equal to 0.999 is denoted as $\zeta_n = \zeta_B$. With the instantaneous pressure evaluated at $\zeta_n = \zeta_B$, $P(\zeta_B)$, the local pressure jump is written as $\Delta P = P(\zeta_B) - P_F$. Here, ΔP represents a pressure jump along a line that passes one point on the shock surface and fluctuates when the shock wave propagates in turbulence. On the other hand, $P_B - P_F$ represents the mean pressure jump across the shock wave and is used to determine the ζ_n location where the local pressure jump is evaluated. This evaluation of ΔP is validated by comparing the statistics of ΔP with experiments below. The pressure jump $\Delta P(y, z)$ is evaluated for various locations on the shock surface. Finally, the local shock Mach number $M_S(y, z)$ is calculated from the

Local geometry of a weak normal shock wave interacting in turbulence

Rankine–Hugoniot relations as

$$M_S = \sqrt{\frac{\gamma+1}{2\gamma}\frac{\Delta P}{P_F}+1}. \tag{16}$$

C. Statistics of the shock wave

Statistics are evaluated for the shock wave propagating in turbulence because the interaction with turbulence causes fluctuations in the shock wave properties. For variables related to the shock wave, such as the curvatures and local shock Mach number, the statistics are calculated with averages taken on the shock surface, whose location is given by $x_S(y,z)$. The statistics of the shock wave depend on time, and the average is denoted by $\langle f\rangle(t)$. The rms value of the fluctuations $f' = f - \langle f\rangle$ is calculated as $f'_{rms} = \sqrt{\langle f^2\rangle - \langle f\rangle^2}$. Here, the rms value is evaluated for each snapshot as a function of time.

In addition, the statistics near the shock wave are evaluated as functions of the distance from the mean position of the shock wave, $\langle x_S\rangle$. Because of the statistical homogeneity in the y and z directions, the averages of flow variables are taken on y–z planes as functions of x and t. This average is denoted by $\overline{f}$. Then, the results are plotted against the streamwise position with respect to $\langle x_S\rangle$, $\Delta x_S = x - \langle x_S\rangle$. For this definition, $\Delta x_S > 0$ represents the front of the shock wave whereas $\Delta x_S < 0$ is located behind the shock wave.

Once the shock wave propagates into the turbulent region, the local pressure jump across the shock wave begins to fluctuate, resulting in $\Delta P' = \Delta P - \langle \Delta P\rangle \neq 0$. Experiments and numerical simulations have shown that the statistics of $\Delta P'$ become statistically steady.[23,27] For the present values of the shock Mach number, the rms value of $\Delta P'$, $\Delta P'_{rms} = \langle \Delta P'^2\rangle^{1/2}$, normalized by the mean pressure jump $\langle \Delta P\rangle$ at the steady state is expected to obey a power law of $M_{T0}^2/(M_{S0}^2-1)$, for which an exponent of 0.5 can be derived with the shock deformation model.[33] Figure 4 presents the relation between $\Delta P'_{rms}/\langle \Delta P\rangle$ and $M_{T0}^2/(M_{S0}^2-1)$ in the statistically steady state of the present DNS. The line indicates $\Delta P'_{rms}/\langle \Delta P\rangle = 0.669[M_{T0}^2/(M_{S0}^2-1)]^{0.489}$, which is obtained with the least square method applied to the data taken from other experiments and numerical simulations. The present results are in good agreement with the power law. This comparison indicates that the interaction of the shock wave with turbulence is well reproduced in the DNS and that the shock wave properties are correctly evaluated with the post-processing procedure discussed above.

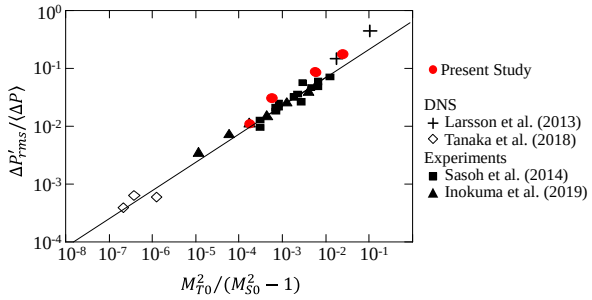

FIG. 4. Normalized rms fluctuations of the pressure jump across shock waves, $\Delta P'_{rms}/\langle\Delta P\rangle$, plotted against $M^2_{T0}/(M^2_{S0}-1)$. Steady-state values in the present DNS are compared with experiments of shock waves in grid turbulence by Sasoh et al.[25] and Inokuma et al.[33] and DNS of shock waves in isotropic turbulence by Larsson et al.[21] and Tanaka et al.[23] The line indicates the power law $\Delta P'_{rms}/\langle\Delta P\rangle = 0.669[M^2_{T0}/(M^2_{S0}-1)]^{0.489}$, which was obtained with a least square method applied to experimental and numerical data in Inokuma et al.[33]

D. Governing equation for pressure

The local shock Mach number is related to the pressure jump across the shock wave. The variation of pressure at the shock wave is examined with the internal energy equation, which can be rewritten as the transport equation for pressure P:

$$\frac{DP}{Dt} = -\gamma P\frac{\partial u_j}{\partial x_j} + (\gamma-1)\frac{\partial}{\partial x_j}\left(k_T\frac{\partial T}{\partial x_j}\right) + (\gamma-1)\tau_{ij}\frac{\partial u_i}{\partial x_j} = \Theta_P + D_T + \varepsilon_P, \qquad (17)$$

where Θ_P is the pressure-dilatation correlation term, which represents the conversion between the kinetic energy and internal energy by compression or expansion of fluids,[60] D_T is the thermal diffusion term, and ε_P represents an increase of the internal energy due to the viscous dissipation of the kinetic energy. Because of the compression due to the shock wave, the kinetic energy is converted to the internal energy by Θ_P. A flow in the shock propagation direction is induced behind the shock wave. This induced flow causes a large velocity gradient within the shock wave, which enhances the normal viscous stress τ_{xx}. Therefore, the energy conversion between the kinetic and internal energies by the viscous effects, ε_P, is also expected to be important in the pressure increase due to the shock wave. On the other hand, the diffusion term can contribute to the spatial transfer of internal energy across the

shock wave because of the large internal energy behind the shock wave caused by the other two terms.

The pressure-dilatation correlation term Θ_P contains the divergence of the velocity vector, $\partial u_j/\partial x_j$, which can be decomposed into three components in an orthogonal coordinate system, e.g., $\partial u_j/\partial x_j = \partial u/\partial x + \partial v/\partial y + \partial w/\partial z$ in the reference frame of the DNS. The decomposition of $\partial u_j/\partial x_j$ is applied with the velocity components in the reference frame related to the local shock geometry. Here, the normal direction and the tangential directions of the principal curvatures are given by $\boldsymbol{e}_n$, $\boldsymbol{e}_{t1}$, and $\boldsymbol{e}_{t2}$, respectively, which can uniquely define the coordinate system of $(\zeta_n, \zeta_{t1}, \zeta_{t2})$. The corresponding velocity vectors are denoted by (u_n, u_{t1}, u_{t2}). Then, Θ_P is decomposed into the following three terms:

$$\Theta_P = -\gamma P\frac{\partial u_n}{\partial \zeta_n} - \gamma P\frac{\partial u_{t1}}{\partial \zeta_{t1}} - \gamma P\frac{\partial u_{t2}}{\partial \zeta_{t2}} = \Theta_{Pn} + \Theta_{Pt1} + \Theta_{Pt2}. \tag{18}$$

For an undisturbed normal shock wave, Θ_{Pt1} and Θ_{Pt2} are zero, and the pressure jump across the shock wave is related to the normal component Θ_{Pn}. However, the tangential components are expected to partially contribute to the fluctuations in the pressure jump once the shock wave interacts with turbulence.

IV. RESULTS AND DISCUSSION

A. The deformation of the shock wave interacting with turbulence

The transient behavior of the interaction of the shock wave with turbulence is examined with the temporal variations of the shock wave statistics. Here, the statistics of the shock wave $\langle f\rangle(t)$ are plotted as a function of the mean shock position $\langle x_S\rangle(t)$. Figures 5(a) and (b) show the rms fluctuations of H and M_S, denoted by H'_{rms} and M'_{Srms}, respectively. Here, H'_{rms} and M'_{Srms} are normalized by the Kolmogorov scale of turbulence, η, and the mean shock Mach number $\langle M_S\rangle$, respectively. As the shock wave initially has $H = 0$ and $M_S = M_{S0}$ without fluctuations, H'_{rms} and M'_{Srms} rapidly increase from zero around $\langle x_S\rangle/L_0 = 2.5$, where the shock wave begins to interact with turbulence. In Fig. 5(b), an increase of M'_{Srms} becomes slightly slower at $\langle x_S\rangle/L_0 \approx 3$ just after the rapid initial increase. Around this position, M'_{Srms} for $M_{T0} = 0.011$ slightly decreases as the shock wave propagates. Then, M'_{Srms} increases again. At the initial phase of the interaction, the shock wave passes the interfacial region that separates turbulence from the outer non-turbulent region with small

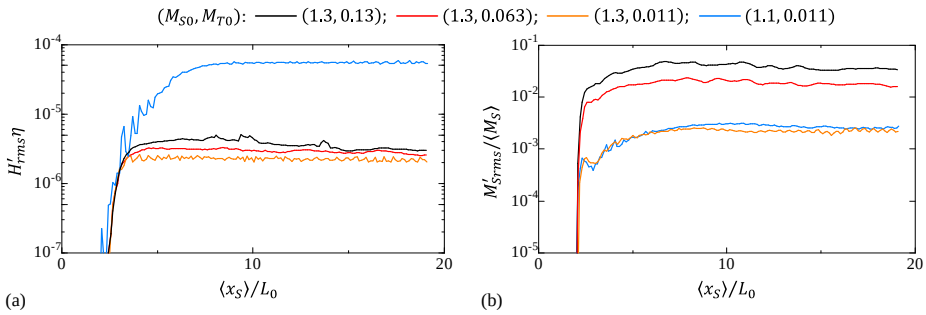

FIG. 5. Variations of rms fluctuations of (a) the mean curvature H, H'_{rms}, and (b) the local shock Mach number M_S, M'_{Srms}, which are plotted against the mean shock wave position $\langle x_S \rangle / L_0$. The Kolmogorov scale η and the mean shock Mach number $\langle M_S \rangle$ are used for the normalization of H'_{rms} and M'_{Srms}, respectively.

velocity fluctuations. The shock wave may behave differently in the interfacial region because the flow near the turbulent/non-turbulent interface is very different from a fully developed turbulence.[61–63] After the shock wave propagates for a sufficiently long distance, H'_{rms} and M'_{Srms} reach a statistically steady state. The normalized values of H'_{rms} and M'_{Srms} in the steady state depend on the shock and turbulent Mach numbers. The results for $M_{S0} = 1.3$ suggest that $H'_{rms}\eta$ and $M'_{Srms}/\langle M_s \rangle$ increase as M_{T0} increases. For a fixed value of $M_{T0} = 0.011$, the normalized rms fluctuations are smaller for a higher shock Mach number although this difference is subtle for $M'_{Srms}/\langle M_s \rangle$. Thus, turbulence tends to have greater influences on the shock wave for larger M_{T0} and smaller M_{S0}. Large M_{T0} and small M_{S0} imply that the shock wave is relatively weak compared to the turbulent velocity fluctuations. Hereafter, the shock wave in the statistically steady state between $\langle x_S \rangle / L_0 = 13$ and 19 is analyzed.

Figure 6 visualizes the mean and Gaussian curvatures, H and K, of the shock surface for $(M_{S0}, M_{T0}) = (1.3, 0.063)$. Thin and long regions with large H are found in Fig. 6(a). These regions tend to have negative K in Fig. 6(b). Therefore, a saddle shape with large curvature appears along curved lines on the shock surface. Circular spots with large positive K are also found in Fig. 6(b). These regions can have both positive and negative values of H in Fig. 6(a). Therefore, both elliptic concave and convex shapes exist on the shock surface. Otherwise, the correlation between the signs of K and H is not prominent and

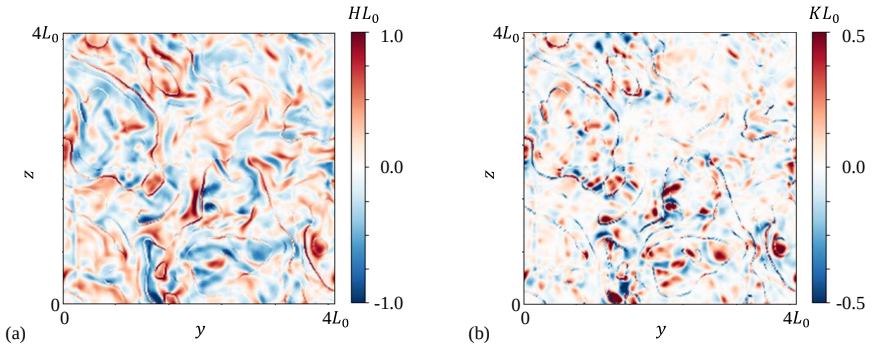

FIG. 6. Visualization of the surface geometry of the shock wave: (a) the mean curvature H and (b) the Gaussian curvature K. Color contours of H and K are shown on a y–z plane for the shock wave in a statistically steady state for $(M_{S0}, M_{T0}) = (1.3, 0.063)$.

various shapes are observed on the shock surface.

Figure 7(a) shows a joint probability density function (PDF) between H and K for $(M_{S0}, M_{T0}) = (1.3, 0.063)$. The PDF in the other cases has a similar distribution. The PDF has the largest value for small negative K with $H \approx 0$, and the PDF decreases as $|H|$ and $|K|$ increase. Therefore, a large part of the shock surface has an approximately-flat saddle shape. The probability for large $|H|$ tends to be large for positive K, and the region with a large mean curvature often has an elliptic shape. Figure 7(b) shows the PDFs of H and K for the same case as in the joint PDF. Skewness and flatness of a variable f are defined as $S(f) = \langle f'^3\rangle/\langle f'^2\rangle^{3/2}$ and $F(f) = \langle f'^4\rangle/\langle f'^2\rangle^2$, respectively. For the PDF shown in Fig. 7(b), we have obtained $S(H) = -0.1$, $F(H) = 8.7$, $S(K) = 1.3$, and $F(K) = 84.9$. When a probability distribution follows a Gaussian function, the skewness and flatness are 0 and 3, respectively. The deviation of $F(H)$ and $F(K)$ from 3 suggests that very large curvatures intermittently appear on the shock surface. This is also anticipated from Fig. 6, where thin lines and approximately-circular spots with large $|H|$ and $|K|$ occupy a small fraction of the shock surface. For the mean curvature, $S(H)$ is close to 0, and there is no preference for the surface to be concave or convex. However, positive $S(K)$ indicates that an elliptic shape with a very large curvature forms on the surface at a low probability, as also confirmed as circular spots with large positive K in Fig. 6(b).

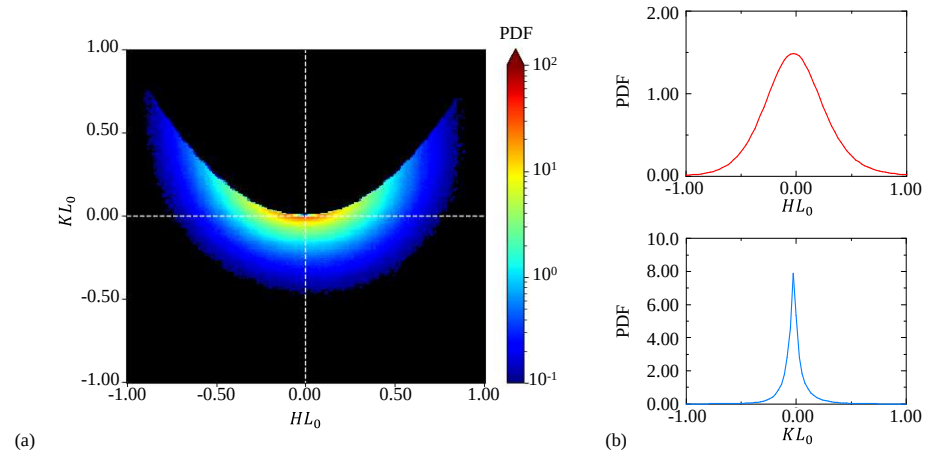

FIG. 7. (a) Joint PDF between H and K and (b) PDFs of H and K for $(M_{S0}, M_{T0}) = (1.3, 0.063)$. The PDF, H, and K are normalized by L_0.

The joint PDF suggests that various shapes illustrated in Fig. 3 are observed for the shock surface. The relationship between the shock wave properties and the local surface geometry is examined with conditional averages with (H, K). Here, an average of a variable f is taken conditionally on values of H and K, and is denoted by $\langle f|H, K\rangle$. For a range of (H, K) with a very small joint PDF, the number of samples is not sufficient to obtain well-converged statistics. Therefore, the conditional statitsics are examined for $(H/H'_{rms}, K/K'_{rms})$ with the joint PDF exceeding 0.1.

Figure 8 plots the conditional average of the shock Mach number $\langle M_S|H, K\rangle$ on a H–K plane for $(M_{S0}, M_{T0}) = (1.3, 0.063)$ and $(1.3, 0.011)$. Here, we have omitted the results for other cases because the plots are similar. The conditional average is shown as a deviation from the conventional mean value, $\Delta M_S = \langle M_S|H, K\rangle - \langle M_S\rangle$, which is normalized by the rms value of fluctuations, M'_{Srms}. Positive and negative values of ΔM_S are found for $H > 0$ and $H < 0$, respectively. In addition, ΔM_S becomes large in magnitude for $K > 0$. Therefore, the shock waves with elliptic concave and convex shapes tend to be locally strong and weak, respectively. The strong shock wave for $H > 0$ is consistent with the focusing effect expected for a concave shape, which has been discussed in Sec. I. Similarly, the weak

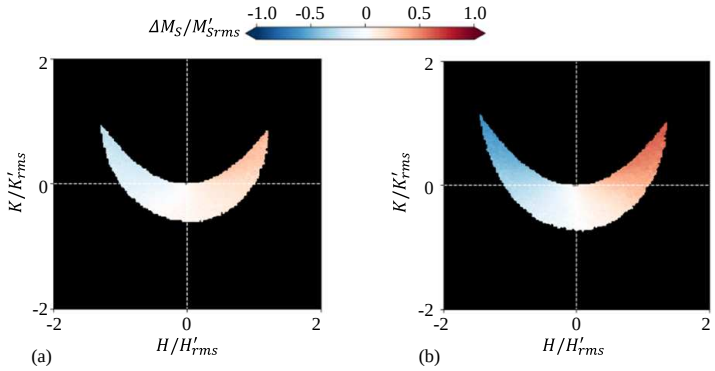

FIG. 8. The conditional average of the local shock Mach number $\langle M_S|H,K\rangle$, which is plotted as a deviation from the conventional average normalized by the rms fluctuations, $\Delta M_S/M'_{Srms} = (\langle M_S|H,K\rangle - \langle M_S\rangle)/M'_{Srms}$ on a H–K plane. The results are obtained in the statistically steady state for (a) $(M_{S0}, M_{T0}) = (1.3, 0.063)$ and (b) $(1.3, 0.011)$.

shock wave for $H < 0$ is also consistent with the defocusing effect for a convex shape. Therefore, the present results support the assumption of the shock deformation model for the shock wave modulation by turbulence.[33]

B. The relation of the local surface geometry to amplification and attenuation of the shock wave

The governing equation for pressure, Eq. (17), is analyzed near the shock wave. Figure 9 plots the averages of DP/Dt, Θ_P, D_T, and ε_P as a distance from the mean shock wave position, Δx_S, for $(M_{S0}, M_{T0}) = (1.3, 0.063)$. A large peak in the average of DP/Dt contributes to the pressure jump across the shock wave. As expected for the compressive nature of shock waves, Θ_P has a dominant contribution to DP/Dt. Therefore, the dependence of Θ_P on the shock surface geometry is discussed below.

Figure 10 shows the conditional average of Θ_P on (H,K), $\langle\Theta_P|H,K\rangle$, for $(M_{S0}, M_{T0}) = (1.3, 0.063)$ and $(1.3, 0.011)$. Here, the color contour shows a deviation from the average, $\Delta\Theta_P = \langle\Theta_P|H,K\rangle - \langle\Theta_P\rangle$, normalized by the rms fluctuations of Θ_P, $(\Theta_P)'_{rms} =$

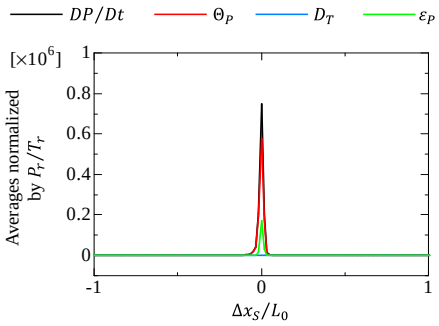

FIG. 9. Averages of Eq. (17) plotted against the distance from the mean position of the shock wave, $\Delta x_S = x - \langle x_S \rangle$, for $(M_{S0}, M_{T0}) = (1.3, 0.063)$. All terms are normalized by the reference values of pressure and time, which are given by $P_r = \rho_0 (u'_{rms0})^2$ and $T_r = L_0/u'_{rms0}$.

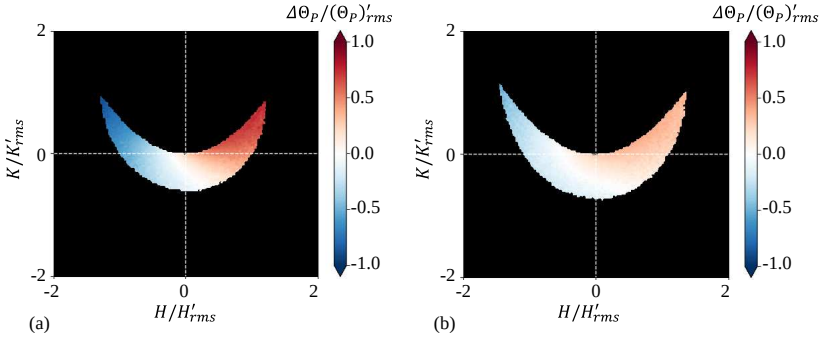

FIG. 10. The conditional average of the pressure-dilatation correlation term Θ_P, $\langle \Theta_P | H, K \rangle$, at the shock wave for (a) $(M_{S0}, M_{T0}) = (1.3, 0.063)$ and (b) $(1.3, 0.011)$. The conditional average is shown as a deviation from the conventional average, $\Delta\Theta_P = \langle \Theta_P | H, K \rangle - \langle \Theta_P \rangle$, which is normalized by the rms fluctuations of Θ_P, $(\Theta_P)'_{rms} = \sqrt{\langle \Theta_P^2 \rangle - \langle \Theta_P \rangle^2}$.

$\sqrt{\langle \Theta_P^2 \rangle - \langle \Theta_P \rangle^2}$. The dependence of $\langle \Theta_P | H, K \rangle$ on (H, K) is similar to that of the shock Mach number: positive and negative values of $\Delta\Theta_P$, corresponding to strong and weak shock waves, are observed for $H > 0$ and $H < 0$, respectively. This is especially true for $K > 0$, which represents elliptic shapes. Thus, the shock wave is significantly amplified and

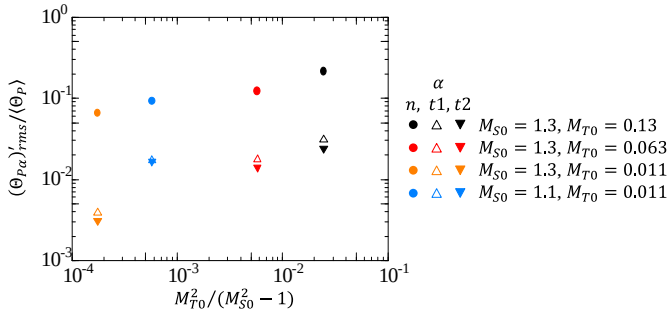

FIG. 11. A comparison of rms fluctuations of the decomposed terms of the pressure-dilatation correlation, $(\Theta_{Pn})'_{rms}$, $(\Theta_{Pt1})'_{rms}$, and $(\Theta_{Pt2})'_{rms}$, which are normalized by the average of Θ_P. The normalized rms fluctuations are plotted as functions of $M_{T0}^2/(M_{S0}^2-1)$.

attenuated for elliptic concave and convex shapes, respectively.

C. Compression and expansion in the normal and tangential directions of the shock surface

The decomposition of Θ_P, Eq. (18), is applied on the shock surface. Figure 11 plots the rms values of Θ_{Pn}, Θ_{Pt1}, and Θ_{Pt2} normalized by the average of Θ_P as functions of $M_{T0}^2/(M_{S0}^2-1)$. The rms fluctuations of the pressure jump normalized by the mean pressure jump increase with $M_{T0}^2/(M_{S0}^2-1)$. Similarly, the normalized rms fluctuations of Θ_{Pn}, Θ_{Pt1}, and Θ_{Pt2} tend to increase with $M_{T0}^2/(M_{S0}^2-1)$. As the pressure jump is caused by large positive Θ_P at the shock wave, larger fluctuations in Θ_P result in larger fluctuations in the pressure jump. The normal component Θ_{Pn} has larger fluctuations than the tangential components, Θ_{Pt1}, and Θ_{Pt2}, which have similar values of the rms fluctuations. Specifically, the rms fluctuations of Θ_{Pt1} and Θ_{Pt2} are about 10% of that of Θ_{Pn}.

The dependence of Θ_{Pn}, Θ_{Pt1}, and Θ_{Pt2} on the shock surface geometry is examined with the conditional averages. Figure 12 shows the conditional average of the shock-normal component, $\langle\Theta_{Pn}|H,K\rangle$, which is shown as a normalized deviation from the average, $\Delta\Theta_{Pn}/(\Theta_{Pn})'_{rms} = (\langle\Theta_{Pn}|H,K\rangle - \langle\Theta_{Pn}\rangle)/(\Theta_{Pn})'_{rms}$. The color contour shows that $\Delta\Theta_{Pn}$ tends to be positive and negative for $H > 0$ and $H < 0$, respectively. The shock wave causes

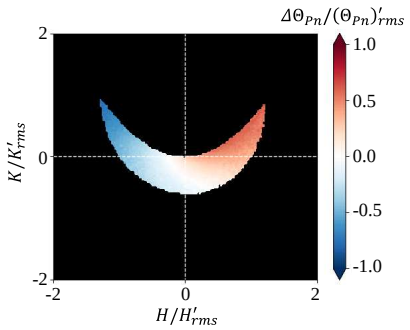

FIG. 12. The conditional average of the normal component of the pressure-dilatation correlation term, $\langle\Theta_{Pn}|H,K\rangle$, for $(M_{S0},M_{T0})=(1.3,0.063)$. The conditional average is shown as the normalized deviation from the average, $\Delta\Theta_{Pn}/(\Theta_{Pn})'_{rms}=(\langle\Theta_{Pn}|H,K\rangle-\langle\Theta_{Pn}\rangle)/(\Theta_{Pn})'_{rms}$.

strong fluid compression in the propagation direction, which is the normal direction of the surface. Therefore, the dependence on (H,K) is similar for Θ_{Pn} and M_S, both of which become larger and smaller than the averages for $H>0$ and $H<0$, respectively. For the same reason, $\Delta\Theta_{Pn}$ is large in magnitude for large $|H|$ with elliptic shapes ($K>0$), as also found for the shock Mach number.

Figures 13 shows the deviation of the conditional averages of the tangential components, $\Delta\Theta_{Pt1}=\langle\Theta_{Pt1}|H,K\rangle-\langle\Theta_{Pt1}\rangle$ and $\Delta\Theta_{Pt2}=\langle\Theta_{Pt2}|H,K\rangle-\langle\Theta_{Pt2}\rangle$, which are also normalized by their rms fluctuations. Positive and negative values of $\Delta\Theta_{Pt1}$ are observed for $H>0$ and $H<0$, respcetively. The pressure jump of the shock wave is increased by compression in the $\boldsymbol{e}_{t1}$ direction for $H>0$ whereas it is reduced by expansion for $H<0$. On the other hand, $\Delta\Theta_{Pt2}$ is mostly negative, and the velocity gradient in the $\boldsymbol{e}_{t2}$ direction causes fluid expansion, which reduces the pressure jump of the shock wave. However, $\Delta\Theta_{Pt2}$ is positive for $H>0$ with $K\approx H^2$, which is the upper bound of K for the surface. For $K\approx H^2$, the curvatures in the $\boldsymbol{e}_{t1}$ and $\boldsymbol{e}_{t2}$ directions satisfy $\kappa_1\approx\kappa_2$, and the surface has an elliptic concave or convex shape with an equal curvature in all directions. Therefore, the physical meaning is similar for the two principal directions of $\boldsymbol{e}_{t1}$ and $\boldsymbol{e}_{t2}$. Thus, both $\Delta\Theta_{Pt1}$ and $\Delta\Theta_{Pt2}$ are positive for $K\approx H^2$ with $H>0$.

Figure 14 summarizes the relationship between the shock surface geometry and the

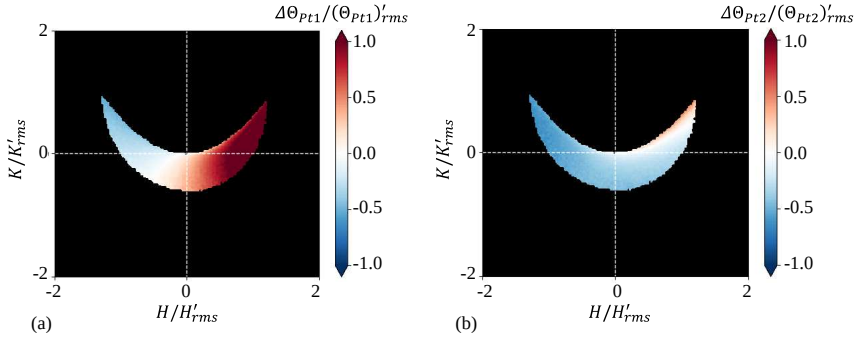

FIG. 13. The conditional averages of the tangential components of the pressure-dilatation correlation term, (a) $\langle\Theta_{Pt1}|H,K\rangle$ and (b) $\langle\Theta_{Pt2}|H,K\rangle$, for $(M_{S0},M_{T0})=(1.3,0.063)$. The conditional averages are shown as the normalized deviations from the averages, $\Delta\Theta_{Pt1}/(\Theta_{Pt1})'_{rms}=(\langle\Theta_{Pt1}|H,K\rangle-\langle\Theta_{Pt1}\rangle)/(\Theta_{Pt1})'_{rms}$ and $\Delta\Theta_{Pt2}/(\Theta_{Pt2})'_{rms}=(\langle\Theta_{Pt2}|H,K\rangle-\langle\Theta_{Pt2}\rangle)/(\Theta_{Pt2})'_{rms}$.

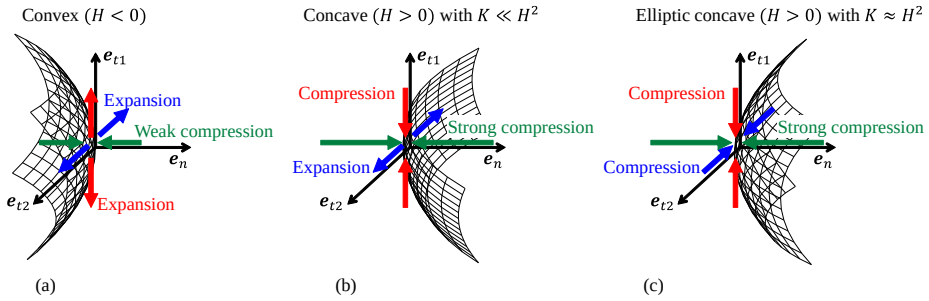

FIG. 14. The relation between the shock surface geometry and the behavior of the shock wave. (a) a convex shape with $H<0$; (b) a concave shape with $H>0$; (c) an elliptic concave shape with $H>0$ and $K\approx H^2$.

pressure-dilatation correlation term, which can be related to the local shock Mach number. The present results qualitatively agree with the shock deformation model for the shock/turbulence interaction,[32,33] for which concave and convex shapes cause amplification and attenuation of the shock wave, respectively. Here, the directions of the principal curvatures κ_1 and κ_2 with $\kappa_1>\kappa_2$ are respectively denoted by $\boldsymbol{e}_{t1}$ and $\boldsymbol{e}_{t2}$. The shock wave behaves

differently for convex and concave shapes, for which the mean curvature $H = (\kappa_1 + \kappa_2)/2$ is negative and positive, respectively. Except for $K \approx H^2$, this H dependence is generally observed for both saddle and elliptic shapes, for which the Gaussian curvature $K = \kappa_1\kappa_2$ is negative and positive, respectively. The H dependence of the shock wave is illustrated in Figs. 14(a, b). Here, elliptic shapes with $K > 0$ are shown in the figures although a shock wave with a saddle shape with $K < 0$ behaves similarly. When H is negative as shown in Fig. 14(a), the shock surface has a convex shape in the $\boldsymbol{e}_{t2}$ direction for $K < 0$ (saddle convex) or in both $\boldsymbol{e}_{t1}$ and $\boldsymbol{e}_{t2}$ directions for $K > 0$ (elliptic convex). The shock wave for this case is accompanied by fluid expansion in the $\boldsymbol{e}_{t1}$ and $\boldsymbol{e}_{t2}$ directions, which contributes to the reduction of the pressure jump. This can also result in the reduction of the shock Mach number, by which fluid compression in the shock normal direction (Θ_{Pn}) becomes weak. Figure 14(b) shows an example of a concave shape with $H > 0$ and $K \ll H^2$. For this case, the compression in the $\boldsymbol{e}_{t1}$ direction and expansion in the $\boldsymbol{e}_{t2}$ direction contribute to the amplification and reduction of the pressure jump, respectively. Because of the definition of H with $\kappa_1 > \kappa_2$, the curvature is larger in magnitude in the $\boldsymbol{e}_{t1}$ direction than in the $\boldsymbol{e}_{t2}$ direction regardless of the sign of κ_2. Therefore, the compression associated with the concave shape in the $\boldsymbol{e}_{t1}$ direction becomes dominant, resulting in the amplification of the shock wave. This is indeed confirmed by a large shock Mach number for $H > 0$, which causes the strong compression in the shock normal direction, i.e., large Θ_{Pn}. However, tangential compression occurs in both $\boldsymbol{e}_{t1}$ and $\boldsymbol{e}_{t2}$ directions for $H > 0$ with $K \approx H^2$. This case corresponds to $\kappa_1 \approx \kappa_2 > 0$, for which the surface has an elliptic concave shape with equal curvatures in the $\boldsymbol{e}_{t1}$ and $\boldsymbol{e}_{t2}$ directions. Therefore, the compression for the concave shape acts in these two tangential directions, as illustrated in Fig. 14(c). This also results in the strongest compression in the normal direction and the largest shock Mach number for $K \approx H^2$ with $H > 0$ in Figs. 8 and 12. For the same reason, the significant tangential expansion occurs for $H < 0$ with $K \approx H^2$, which represents an elliptic convex shape with equal curvatures in the $\boldsymbol{e}_{t1}$ and $\boldsymbol{e}_{t2}$ directions. Therefore, this geometry is associated with the weakest compression in the normal direction and the smallest shock Mach number.

These relations between the geometry and the compression and expansion in the tangential directions can be explained by a flow induced by the deformed shock wave. The velocity vector of the induced flow is locally perpendicular to the shock wave. Figure 15 shows the sketches of the induced flows behind a deformed shock wave in a two-dimensional plane,

Local geometry of a weak normal shock wave interacting in turbulence

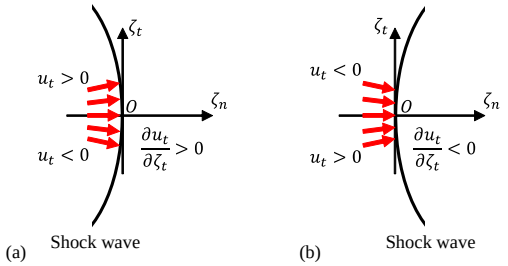

FIG. 15. Flows induced by a shock wave with (a) convex and (b) concave shapes.

where ζ_n and ζ_t are the coordinates in the normal and tangential directions of the shock wave and $(\zeta_n, \zeta_t) = (0, 0)$ is located on the shock surface. Although the explanation is given for the two-dimensional flow, it is also valid for three-dimensional cases. The velocity vector of the induced flow behind the shock wave does not align with the ζ_n direction because of the curved geometry of the shock wave. Therefore, the induced velocity in the tangential direction u_t is not zero. For the convex shape shown in Fig. 15(a), the induced flow has $u_t > 0$ for $\zeta_t > 0$ and $u_t < 0$ for $\zeta_t < 0$, resulting in $\partial u_t/\partial \zeta_t > 0$. Thus, the diverging induced flow behind the shock wave can cause fluid expansion in the tangential direction of the shock wave. Conversely, the induced flow for the concave shape has opposite signs of u_t as shown in Fig. 15(b), and fluid compression in the tangential direction is therefore caused by $\partial u_t/\partial \zeta_t < 0$. The induced flow tilted from the ζ_n direction is related to the divergent and convergent shock rays of the deformed shock waves discussed in Sec. I. The flow illustrated in Fig. 15, based on the present DNS results, is compared well with the shock-deformation model in Inokuma et al.[32,33] The model considers the divergent and convergent shock rays for convex and concave shapes, respectively, where the deformation of the shock wave is assumed to be caused by velocity fluctuations in turbulence. The model predicts the behaviour of a deformed shock wave based on the integral properties in a control area on the shock surface enclosed by shock rays. This approach was originally proposed in an early theoretical study of a shock wave in a non-uniform tube.[64] Although this integral approach with the control area is useful to discuss temporal variations in the shock Mach number, it does not reveal the underlying mechanism of the interaction between shock waves and

turbulence. The present results for Θ_{Pt1} and Θ_{Pt2} explain the influences of these shock rays tilted from the mean propagation direction with compression and expansion in the shock tangential direction, whose influence on the shock Mach number is consistent with the model, as discussed with the conditional average of the shock Mach number in Fig. 8. In addition, a quantitative comparison with the model has also been provided in Fig. 4, where the line that approximates the plots is consistent with the power law obtained with the model. This comparison indicates that the model successfully explains the DNS results for the change in the shock wave due to the interaction with turbulence.

V. CONCLUSIONS

The DNS database of a normal shock wave propagating into a local turbulent region has been analyzed to investigate the local surface geometry of the shock wave interacting with turbulence. The initial shock and turbulent Mach numbers are $(M_{S0}, M_{T0}) = (1.3, 0.13)$, $(1.3, 0.063)$, $(1.3, 0.011)$, and $(1.1, 0.011)$, for which the shock wave retains its surface without holes. The surface geometry of the shock wave is quantified with the mean curvature $H = (\kappa_1 + \kappa_2)/2$ and Gaussian curvature $K = \kappa_1\kappa_2$, which are defined with the principal curvatures κ_1 and κ_2 of the surface. The relation between the local surface geometry and the shock Mach number is examined with conditional averages on (H, K).

Even though the shock wave initially has a flat surface, the surface is deformed by interaction with turbulence. The rms fluctuations of H rapidly increase once the shock wave interacts with turbulence. A comparison among the cases with different parameters confirms that the rms fluctuations of H are larger for higher M_{T0} and for lower M_{S0}. Thus, the shock wave deforms more when turbulence is relatively stronger than the shock wave in terms of the shock and turbulent Mach numbers. A large part of the shock surface has an approximately-flat saddle shape. However, H tends to be very large in magnitude for $K > 0$, indicating that elliptic concave and convex shapes with very large curvatures also appear on the shock surface.

The conditional averages on (H, K) have been evaluated for the local shock Mach number M_S and the pressure-dilatation correlation term Θ_P in the transport equation for pressure. The shock Mach number is positively correlated with the mean curvature, and the shock wave is locally strong and weak for the concave and convex shapes, respectively. Consistently,

Θ_P associated with the pressure increase at the shock wave tends to be large and small for the concave and convex shapes, respectively. In addition, Θ_P is decomposed into the three components of the velocity gradients related to the normal direction and two tangential directions of the principal curvatures of the shock surface. The tangential components have been shown to strongly depend on the mean curvature. Fluid expansion in the tangential direction occurs at the shock wave with a convex shape, resulting in a smaller pressure jump across the shock wave. For a concave shape, compression in the tangential direction can amplify the pressure jump. Consistently, the concave and convex shapes are associated with large and small local shock Mach numbers, respectively. These differences in the local shock Mach number are also related to strong and weak compression in the shock normal direction observed for the concave and convex shapes, respectively. Because these geometric influences are the most significant for elliptic concave and convex shapes with approximately equal curvatures in the two principal directions, the shock Mach number becomes the largest and smallest for the elliptic shapes. These compression and expansion in the tangential directions have been explained by the flow induced behind the shock wave: the shock wave with a concave shape induces a converging flow with the compression behind the shock wave whereas a diverging flow with the expansion is induced for a convex shape. These observations based on the DNS support the shock deformation model recently proposed for the shock wave modulation due to turbulence and will be useful for constructing phenomenological models for the interaction between shock waves and turbulence in future studies.

ACKNOWLEDGMENTS

This work was supported by the Collaborative Research Project on Computer Science with High-Performance Computing in Nagoya University and by JSPS KAKENHI Grant Nos. JP21H04589 and JP22K03903.

AUTHOR DECLARATIONS

Conflict of interest

The authors have no conflicts to disclose.

Author Contributions

Amane Kusuhata: Data Curation (lead); Formal Analysis (lead); Investigation (lead); Methodology (equal); Software (equal); Validation (equal); Visualization (lead); Writing/Original Draft Preparation (equal); Writing/Review & Editing (equal). **Kento Tanaka**: Data Curation (supporting); Formal Analysis (supporting); Investigation (supporting); Methodology (supporting); Software (equal); Validation (equal); Writing/Review & Editing (supporting). **Tomoaki Watanabe**: Conceptualization (lead); Data Curation (supporting); Formal Analysis (supporting); Funding Acquisition (supporting); Investigation (supporting); Methodology (equal); Project Administration (equal); Resources (equal); Software (equal); Supervision (equal); Validation (supporting); Visualization (supporting); Writing/Original Draft Preparation (equal); Writing/Review & Editing (equal); **Koji Nagata**: Conceptualization (supporting); Formal Analysis (supporting); Funding Acquisition (equal); Investigation (supporting); Methodology (equal); Project Administration (equal); Resources (equal); Supervision (equal); Validation (supporting); Writing/Review & Editing (supporting). **Akihiro Sasoh**: Conceptualization (supporting); Funding Acquisition (equal); Investigation (supporting); Methodology (supporting); Project Administration (supporting); Resources (equal); Supervision (supporting); Writing/Review & Editing (supporting).

DATA AVAILABILITY

The data that support the findings of this study are available from the corresponding author upon reasonable request.

REFERENCES

[1]X.-X. Yan, H.-B. Cai, W.-S. Zhang, L. Hao, P.-L. Yao, X. Li, S.-Y. Zou, S.-P. Zhu, and X.-T. He, "Anomalous mix induced by a collisionless shock wave in an inertial confinement fusion hohlraum," Nucl. Fusion **59**, 106016 (2019).

[2]S. I. Abarzhi, D. L. Hill, K. C. Williams, J. T. Li, B. A. Remington, D. Martinez, and W. D. Arnett, "Fluid dynamic mathematical aspects of supernova remnants," Phys. Fluids **35** (2023).

[3]G. M. Lilley and A. H. Yates, "Some aspects of noise from supersonic aircraft," J. Roy. Aero. Soc. **57**, 396 (1953).

[4]A. Kawasaki, T. Inakawa, J. Kasahara, K. Goto, K. Matsuoka, A. Matsuo, and I. Funaki, "Critical condition of inner cylinder radius for sustaining rotating detonation waves in rotating detonation engine thruster," Proc. Combust. Inst. **37**, 3461 (2019).

[5]C. Cerri, "The effects of sonic boom on the ecological environment," J. Navig. **33**, 296 (1980).

[6]D. J. Maglieri, "Some effects of airplane operations and the atmosphere on sonic-boom signatures," J. Acoust. Soc. Am. **39**, S36 (1966).

[7]M. Kanamori, T. Takahashi, Y. Makino, Y. Naka, and H. Ishikawa, "Comparison of simulated sonic boom in stratified atmosphere with flight test measurements," AIAA J. **56**, 2743 (2018).

[8]T. K. Sengupta, A. G. Roy, A. Chakraborty, A. Sengupta, and P. Sundaram, "Thermal control of transonic shock-boundary layer interaction over a natural laminar flow airfoil," Phys. Fluids **33**, 126110 (2021).

[9]R. Quadros and M. Bernardini, "Numerical investigation of transitional shock-wave/boundary-layer interaction in supersonic regime," AIAA J. **56**, 2712 (2018).

[10]J. Cheng, K. Yang, X. Zheng, C. Shi, C. Zhu, and Y. You, "Analytical model for predicting the length scale of shock/boundary layer interaction with curvature," Phys. Fluids **34**, 111701 (2022).

[11]Y. P. M. Sethuraman, K. Sinha, and J. Larsson, "Thermodynamic fluctuations in canonical shock–turbulence interaction: effect of shock strength," Theor. Comput. Fluid Dyn. **32**, 629 (2018).

[12]Y. P. M. Sethuraman and K. Sinha, "Modeling of thermodynamic fluctuations in canonical shock–turbulence interaction," AIAA J. **58**, 3076 (2020).

[13]C. H. Chen, "Linear analysis on pressure-dilatation behind shock waves," Phys. Fluids **35**, 021701 (2023).

[14]K. Mahesh, S. K. Lele, and P. Moin, "The response of anisotropic turbulence to rapid homogeneous one-dimensional compression," Phys. Fluids **6**, 1052 (1994).

[15]L. Jacquin, C. Cambon, and E. Blin, "Turbulence amplification by a shock wave and rapid distortion theory," Phys. Fluids **5**, 2539 (1993).

[16]T. Kitamura, K. Nagata, Y. Sakai, A. Sasoh, and Y. Ito, "Rapid distortion theory analysis on the interaction between homogeneous turbulence and a planar shock wave," J. Fluid Mech. **802**, 108 (2016).

[17]J. Keller and W. Merzkirch, "Interaction of a normal shock wave with a compressible turbulent flow," Exp. Fluids **8**, 241 (1990).

[18]J. H. Agui, G. Briassulis, and Y. Andreopoulos, "Studies of interactions of a propagating shock wave with decaying grid turbulence: velocity and vorticity fields," J. Fluid Mech. **524**, 143 (2005).

[19]T. Kitamura, K. Nagata, Y. Sakai, A. Sasoh, and Y. Ito, "Changes in divergence-free grid turbulence interacting with a weak spherical shock wave," Phys. Fluids **29**, 065114 (2017).

[20]S. Lee, S. K. Lele, and P. Moin, "Direct numerical simulation of isotropic turbulence interacting with a weak shock wave," J. Fluid Mech. **251**, 533 (1993).

[21]J. Larsson, I. Bermejo-Moreno, and S. K. Lele, "Reynolds- and Mach-number effects in canonical shock-turbulence interaction," J. Fluid Mech. **717**, 293 (2013).

[22]R. Boukharfane, Z. Bouali, and A. Mura, "Evolution of scalar and velocity dynamics in planar shock-turbulence interaction," Shock Waves **28**, 1117 (2018).

[23]K. Tanaka, T. Watanabe, K. Nagata, A. Sasoh, Y. Sakai, and T. Hayase, "Amplification and attenuation of shock wave strength caused by homogeneous isotropic turbulence," Phys. Fluids **30**, 35105 (2018).

[24]J. Kim, A. Sasoh, and A. Matsuda, "Modulations of a weak shock wave through a turbulent slit jet," Shock Waves **20**, 339 (2010).

[25]A. Sasoh, T. Harasaki, T. Kitamura, D. Takagi, S. Ito, A. Matsuda, K. Nagata, and Y. Sakai, "Statistical behavior of post-shock overpressure past grid turbulence," Shock Waves **24**, 489 (2014).

[26]K. Inokuma, T. Watanabe, K. Nagata, and Y. Sakai, "Statistical properties of spherical shock waves propagating through grid turbulence, turbulent cylinder wake, and laminar flow," Phys. Scr. (2019).

[27]K. Aruga, K. Inokuma, T. Watanabe, K. Nagata, and Y. Sakai, "Experimental investigation of interactions between turbulent cylinder wake and spherical shock wave," Phys. Fluids **32**, 016101 (2020).

[28]T. Tamba, G. Fukushima, M. Kayumi, A. Iwakawa, and A. Sasoh, "Experimental investigation of the interaction of a weak planar shock with grid turbulence in a counter-driver

shock tube," Phys. Rev. Fluid **4** (2019).

[29]K. Tanaka, T. Watanabe, and K. Nagata, "Statistical analysis of deformation of a shock wave propagating in a local turbulent region," Phys. Fluids **32**, 096107 (2020).

[30]A. D. Pierce, "Statistical theory of atmospheric turbulence effects on sonic-boom rise times," J. Acoust. Soc. Am. **49**, 906 (1971).

[31]G. Fukushima, J. Wei, S. Ogawa, J. Hagiwara, Y. Nakamura, and A. Sasoh, "Losing the shock wave front profile due to interaction with turbulence," Fluid Dyn. Res. **53**, 025504 (2021).

[32]K. Inokuma, T. Watanabe, K. Nagata, A. Sasoh, and Y. Sakai, "Finite response time of shock wave modulation by turbulence," Phys. Fluids **29**, 51701 (2017).

[33]K. Inokuma, T. Watanabe, K. Nagata, and Y. Sakai, "Statistics of overpressure fluctuations behind a weak shock wave interacting with turbulence," Phys. Fluids **31**, 085119 (2019).

[34]G. B. Whitham, "A new approach to problems of shock dynamics Part 1 Two-dimensional problems," J. Fluid Mech. **2**, 145 (1957).

[35]J. Larsson and S. K. Lele, "Direct numerical simulation of canonical shock/turbulence interaction," Phys. Fluids **21**, 126101 (2009).

[36]G. Fukushima, S. Ogawa, J. Wei, Y. Nakamura, and A. Sasoh, "Impacts of grid turbulence on the side projection of planar shock waves," Shock Waves **31**, 101 (2021).

[37]C. Dopazo, J. Martín, and J. Hierro, "Local geometry of isoscalar surfaces," Phys. Rev. E **76**, 056316 (2007).

[38]M. Wolf, B. Lüthi, M. Holzner, D. Krug, W. Kinzelbach, and A. Tsinober, "Investigations on the local entrainment velocity in a turbulent jet," Phys. Fluids **24**, 105110 (2012).

[39]M. Hayashi, T. Watanabe, and K. Nagata, "The relation between shearing motions and the turbulent/non-turbulent interface in a turbulent planar jet," Phys. Fluids **33** (2021).

[40]R. Jahanbakhshi and C. K. Madnia, "Entrainment in a compressible turbulent shear layer," J. Fluid Mech. **797**, 564 (2016).

[41]T. Watanabe, C. B. da Silva, K. Nagata, and Y. Sakai, "Geometrical aspects of turbulent/non-turbulent interfaces with and without mean shear," Phys. Fluids **29**, 085105 (2017).

[42]C. B. da Silva and R. R. Taveira, "The thickness of the turbulent/nonturbulent interface is equal to the radius of the large vorticity structures near the edge of the shear layer," Phys. Fluids **22**, 121702 (2010).

[43]H. S. Ribner, P. J. Morris, and W. H. Chu, "Laboratory simulation of development of superbooms by atmospheric turbulence," J. Acoust. Soc. Am. **53**, 926 (1973).

[44]P. Holmes, J. L. Lumley, G. Berkooz, and C. W. Rowley, *Turbulence, coherent structures, dynamical systems and symmetry* (Cambridge university press, 2012).

[45]P. J. Schmid, "Dynamic mode decomposition of numerical and experimental data," J. Fluid Mech. **656**, 5 (2010).

[46]O. Terashima, Y. Sakai, and Y. Ito, "Measurement of fluctuating temperature and POD analysis of eigenmodes in a heated planar jet," Exp. Therm. Fluid Sci. **92**, 113 (2018).

[47]M. Takahashi, R. Fukui, K. Tsujimoto, T. Ando, and T. Shakouchi, "Helical structures in a temporally developing round jet in the developed state," Flow, Turbul. and Combust. , 1 (2023).

[48]K. Takamure, Y. Ito, Y. Sakai, K. Iwano, and T. Hayase, "Momentum transport process in the quasi self-similar region of free shear mixing layer," Phys. Fluids **30**, 015109 (2018).

[49]T. Akao, T. Watanabe, and K. Nagata, "Vertical confinement effects on a fully developed turbulent shear layer," Phys. Fluids **34**, 055129 (2022).

[50]H. Zhang, L. Jia, S. Fu, X. Xiang, and L. Wang, "Vortex shedding analysis of flows past forced-oscillation cylinder with dynamic mode decomposition," Phys. Fluids **35** (2023).

[51]A. Cimarelli, G. Cocconi, B. Frohnapfel, and E. De Angelis, "Spectral enstrophy budget in a shear-less flow with turbulent/non-turbulent interface," Phys. Fluids **27**, 125106 (2015).

[52]T. S. Silva, M. Zecchetto, and C. B. da Silva, "The scaling of the turbulent/non-turbulent interface at high Reynolds numbers," J. Fluid Mech. **843**, 156 (2018).

[53]M. R. Petersen and D. Livescu, "Forcing for statistically stationary compressible isotropic turbulence," Phys. Fluids **22**, 116101 (2010).

[54]R. Nagata, T. Watanabe, and K. Nagata, "Turbulent/non-turbulent interfaces in temporally evolving compressible planar jets," Phys. Fluids **30**, 105109 (2018).

[55]Y. Tai, T. Watanabe, and K. Nagata, "Implicit large eddy simulation of passive scalar transfer in compressible planar jet," Int. J. Numer. Methods Fluids **93**, 1183 (2021).

[56]G. B. Whitham, "A new approach to problems of shock dynamics Part 2. Three-dimensional problems," J. Fluid Mech. **5**, 369 (1959).

[57]S. B. Pope, *Turbulent Flows* (Cambridge Univ. Pr., 2000).

[58]Y. Zheng, K. Nagata, and T. Watanabe, "Energy dissipation and enstrophy production/destruction at very low reynolds numbers in the final stage of the transition period

of decay in grid turbulence," Phys. Fluids **33**, 035147 (2021).

[59]S. Kobayashi, *Differential Geometry of Curves and Surfaces* (Springer, 2019).

[60]O. Zeman, "On the decay of compressible isotropic turbulence," Phys. Fluids **3**, 951 (1991).

[61]C. B. da Silva, J. C. R. Hunt, I. Eames, and J. Westerweel, "Interfacial layers between regions of different turbulence intensity," Annu. Rev. Fluid Mech. **46**, 567 (2014).

[62]T. Watanabe, C. B. da Silva, and K. Nagata, "Non-dimensional energy dissipation rate near the turbulent/non-turbulent interfacial layer in free shear flows and shear free turbulence," J. Fluid Mech. **875**, 321 (2019).

[63]T. Watanabe, C. B. da Silva, and K. Nagata, "Scale-by-scale kinetic energy budget near the turbulent/nonturbulent interface," Phys. Rev. Fluids **5**, 124610 (2020).

[64]G. Whitham, "On the propagation of shock waves through regions of non-uniform area or flow," J. Fluid Mech. **4**, 337 (1958).